### mercury over the marginal seas of China and impact assessment on 2 3 the sea-air exchange of mercury 4 5 Xiaofei Qin<sup>1</sup>, Hao Li<sup>2</sup>, Jia Chen<sup>3</sup>, Junjie Wei<sup>4,5</sup>, Hao Ding<sup>4,5</sup>, Xiaohao Wang<sup>3</sup>, Guochen Wang<sup>2</sup>, 6 Chengfeng Liu<sup>2</sup>, Da Lu<sup>2</sup>, Shengqian Zhou<sup>2</sup>, Haowen Li<sup>2</sup>, Yucheng Zhu<sup>2</sup>, Ziwei Liu<sup>2</sup>, Qingyan Fu<sup>6</sup>, Juntao Huo<sup>3</sup>, Yanfen Lin<sup>3</sup>, Congrui Deng<sup>2</sup>, Yisheng Zhang<sup>1\*</sup>, Kan Huang<sup>2, 7, 8,9\*</sup> 7 8 9 <sup>1</sup>School of Environmental and Municipal Engineering, Qingdao University of Technology, Qingdao, 10 China 11 <sup>2</sup>Shanghai Key Laboratory of Atmospheric Particle Pollution and Prevention (LAP<sup>3</sup>), National 12 Observations and Research Station for Wetland Ecosystems of the Yangtze Estuary, Department of 13 Environmental Science and Engineering, Fudan University, Shanghai, China 14 <sup>3</sup>Shanghai Environment Monitoring Center, Shanghai, China 15 <sup>4</sup>Key Laboratory of Environmental Pollution Control Technology of Zhejiang Province, Hangzhou, 16 Zhejiang, China 17 <sup>5</sup>Environmental Science Research & Design Institute of Zhejiang Province, Hangzhou, Zhejiang, 18 19 <sup>6</sup>Shanghai Academy of Environmental Sciences, Shanghai, China 20 <sup>7</sup>Institute of Eco-Chongming, Shanghai, China 21 <sup>8</sup>IRDR ICoE on Risk Interconnectivity and Governance on Weather/Climate Extremes Impact and 22 Public Health, Fudan University, Shanghai, China 23 <sup>9</sup>Observation and Research Station of Huaniaoshan East China Sea Ocean-Atmosphere Integrated 24 Ecosystem, Ministry of Natural Resources, Shanghai, China

Quantification of anthropogenic and marine sources to atmospheric

1

25

2627

28

Abstract

Mercury in the atmosphere is a crucial environmental concern due to its toxicity and ability to travel

Correspondence: huangkan@fudan.edu.cn (Kan Huang); doctorzys@163.com (Yisheng Zhang)

long distances. In the marginal seas, the contributions of terrestrial anthropogenic vs. natural sources on atmospheric mercury have been rarely quantified and their roles in mercury sea-air exchange are not well understood. To address this issue, this study integrated observations from island, cruise, and inland campaigns. The mean concentrations of total gaseous mercury (TGM)TGM were  $2.32 \pm$  $1.02 \text{ ng/m}^3$  (Bohai Sea),  $2.55 \pm 0.55 \text{ ng/m}^3$  (Yellow Sea), and  $2.31 \pm 0.81 \text{ ng/m}^3$  (East China Sea), respectively, with coastal regions exhibiting significantly higher values than open ocean areas due to continental outflows. Positive correlations were observed between TGM total gaseous mercury (TGM) concentrations and environmental parameters such as temperature, relative humidity, and wind speed, indicating the significant influence of natural sources on atmospheric mercury in the marine environment. By utilizing a receptor model and linear regression analysis, a robust method was developed to quantitatively estimate the contribution of anthropogenic and natural sources to TGM. Anthropogenic sources accounted for an average of 59%, 40%, and 2927% of TGM over the Bohai Sea, Yellow Sea, and East China Sea, respectively. The sea-air exchange fluxes of mercury were estimated as 0.17±0.38, 1.10±1.34, and 3.44±3.24 ng m<sup>-2</sup> h<sup>-1</sup> over the three seas above, respectively. Stronger anthropogenic mercury emissions in the northern China partially explained the suppressed sea-air exchange fluxes of mercury in the Bohai Sea. To assess the potential impact of anthropogenic emissions on the sea-air exchange fluxes of mercury, anthropogenic contributions to TGM were artificially removed, then the fluxes would be increased by 207.1% in the Bohai Sea, 33.4% in the Yellow Sea, and 6.5% in the East China Sea, respectively. This study elucidated the role of anthropogenic emissions in shaping the marine atmospheric mercury and the modulation of sea-air exchange fluxes, thereby informing valuable assessments regarding the influence of future reduced anthropogenic mercury emissions on the marine mercury cycle and ecosystems.

52 **1. Introduction** 

29

30

31

32

33 34

35

36

37

38

39

40

41

42 43

44

45

46

47

48

49

50

51

53

54

55

56

57

Mercury is a ubiquitous toxic pollutant that can cycle among atmospheric, aquatic, and terrestrial environments (Mason et al., 2012; Lamborg et al., 2014). Anthropogenic discharge of mercury can be transported into marine atmospheres, subsequently entering oceans via wet and dry depositions, constituting a primary source of marine mercury (Outridge et al., 2018). A fraction of mercury that enters oceans can undergo methylation and bioaccumulate in the food chain, thereby

posing health risks to humans through the consumption of methylmercury-contaminated seafood; another fraction converts to dissolved gaseous mercury and can escape from surface seawater through sea-air exchange processes (Lavoie et al., 2018; Obrist et al., 2018). This sea-air exchange is pivotal to the biogeochemical cycling of mercury, as it influences mercury concentrations in seawater, oceanic mercury accumulation rates, and methylmercury production (Mason et al., 2017; Ci et al., 2016). Simultaneously, the sea-air exchange of mercury represented the largest flux between different environmental media within the global mercury cycle. Previous estimates indicated that the release of gaseous elemental mercury from the global ocean contributed approximately one-third of the global atmospheric mercury emissions (Horowitz et al., 2017).

58

59

60

61

62

63 64

65

66 67

68

69

70

71 72

73

74

75

76

77

78

79

80

81

82

83

84

85

86

Numerous studies have emphasized the impact of anthropogenic sources on marine atmospheric mercury. For instance, one study conducted over the Bohai Sea revealed that the increased concentration of gaseous elemental mercury (GEM) resulted from the long-range transport of mercury released from anthropogenic sources (Wang et al., 2020). An island investigation over the East China Sea showed the outflow from mainland China was the primary contributor to atmospheric GEM (Fu et al., 2018). Cruises campaigns over the East China Sea and South China Sea observed elevated GEM concentrations at sites proximate to mainland China, indicating the prominent influence of terrestrial emissions (Fu et al., 2010; Wang et al., 2016a). Additionally, studies in the Gulf of Mexico, North Atlantic Ocean, and Mediterranean Sea also attributed significant portions of atmospheric mercury to anthropogenic emissions (Obrist et al., 2018). Although isotopic signatures have been widely applied to source apportionment of atmospheric mercury, current isotopic methods still exhibit significant uncertainties due to the poor understanding of isotopic compositions of gaseous elemental mercury emitted from various sources and fractionation processes of Hg isotopes during atmospheric transformations (Fu et al., 2018). Additionally, this approach requires specialized isotopic measurements unavailable for routine monitoring. At present, quantitative analyses of anthropogenic contributions to marine atmospheric mercury remain limited.. Although annual global anthropogenic atmospheric mercury emissions have been approximated to reach 2300 tons, accounting for about one-third of global atmospheric mercury emission (Pirrone et al., 2010; Zhang et al., 2016), the specific contributions to marine atmospheric mercury remained poorly delineated, thereby constraining insights into the oceanic mercury cycling dynamics. In this regard, it is imperative to develop methodologies capable of quantifying the contributions from anthropogenic sources to marine atmospheric mercury, particularly in critical marginal seas, which served as essential biogeochemical interfaces between landmasses and open oceans. Previous studies have indicated that the importance of the mercury cycling in offshore ecosystems approximated that within open oceanic environments (Fitzgerald et al., 2007). Marginal seas functioned not only as natural sinks for terrestrial mercury but also represented significant sources of atmospheric mercury (Ci et al., 2011). Given that China ranks as the foremost global emitter of anthropogenic atmospheric mercury (Pacyna et al., 2016; Pacyna et al., 2010; Zhang et al., 2015), its emissions inevitably exert profound influences on adjacent marginal seas.

87

88

89

90

91

92

93

94

95

96

97 98

99

100101

102

103

104

105

106

107

108109

110

111

112

113

114

115

Anthropogenic inputs influenced not only the concentrations of atmospheric mercury but also the dynamics of mercury sea-air exchange. Given that Hg<sup>0</sup> in the surface oceanic waters frequently exceeded its saturation levels, the prevailing direction of sea-air exchange was predominantly upward, facilitating the efflux of mercury from the ocean to the atmosphere (Andersson et al., 2008b; Mason et al., 2001; Huang and Zhang, 2021). The sea-air exchange of Hg<sup>0</sup> was governed by the concentration gradients at the atmosphere-seawater interface (Soerensen et al., 2013), which were influenced by the spectrum of physical and chemical processes within seawater, as well as meteorological conditions and ambient GEM concentrations (Costa and Liss, 1999; Mason, 2009; Selin, 2009). Previous studies illuminated the direct impact of dissolved gaseous mercury (DGM) in surface waters on Hg<sup>0</sup> fluxes, while photochemical reduction of Hg (II) has been identified as the principal mechanism driving the DGM generation in marine settings (Amyot et al., 1994; Huang and Zhang, 2021). Field measurements observed nocturnal peaks in DGM and Hg<sup>0</sup> fluxes, implying that dark reduction processes may significantly contribute to these dynamics (O'driscoll et al., 2003; Fu et al., 2013). Hg<sup>0</sup> fluxes increased 2-4 folds as a result of strengthened wind speeds coupled with Hg (II) inputs from atmospheric precipitation in the Intertropical Convergence Zone (ITCZ) region (Soerensen et al., 2014). While considerable research has elucidated the factors influencing the mercury sea-air exchange, few studies have comprehensively explored the repercussions of fluctuating GEM concentrations on Hg<sup>0</sup> sea-air dynamics. Given the backdrop of observed annual declines in GEM concentrations( -0.011 ± 0.006 ng m<sup>-3</sup> y<sup>-1</sup>) across most Northern Hemispheric

regions from 2005 to 2020 (Feinberg et al., 2024) and particularly pronounced declines (-0.29 ng m<sup>-3</sup>) in China from 2013 to 2017 (Liu et al., 2019), conducting such study in marginal seas is essential

Under the influence of Chinese mainland emissions, mercury pollution in its adjacent marginal seas, such as the East China Sea, Yellow Sea, and Bohai Sea, exhibited pronounced severity. The East China Sea and Yellow Sea, as semi-enclosed seas, are located in the downwind region of East Asia and serve as a major pathway for the transport of pollutants to the Pacific Ocean. The Bohai Sea, as an inland sea, has received a substantial amount of pollutants from the Chinese mainland, making it one of the most mercury-polluted seas in the world (Luo et al., 2012). By focusing on the marginal seas surrounding China, this study integrated observations from two offshore islands, one research cruise, and a coastal city, to reveal the spatiotemporal distribution characteristics of total gaseous mercury (TGM) and dissolved gaseous mercury (DGM). The impact of oceanic meteorological conditions on the atmospheric mercury over the ocean was explored, particularly examining the effects of anthropogenic sources transported from the mainland. Furthermore, we developed a method to quantify the contributions from anthropogenic sources to marine atmospheric mercury and ultimately assessed how these inputs shaped the mercury sea-air exchange dynamics.

**2. Methods** 

# 2.1 Study area

The study area, illustrated in Figure 1a, encompasses the Bohai Sea (BS), the Yellow Sea (YS), and the East China Sea (ECS). The BS, a shallow inner sea bordered by Liaoning, Hebei, and Shandong provinces, covers around 77×10<sup>3</sup> km<sup>2</sup>. The YS, situated between mainland China and the Korean Peninsula, covers around 38×10<sup>4</sup> km<sup>2</sup>. The ECS, a semi-enclosed marginal sea positioned downwind of East Asia, extends over 77×10<sup>4</sup> km<sup>2</sup>. Field measurements were conducted at Juehua Island (JHI) in the BS, approximately 10 km from Xingcheng City, Liaoning Province. Due to its proximity to the mainland, JHI experienced marked impacts from anthropogenic emissions (Li et al., 2023). Field measurements were also conducted at Huaniao Island (HNI) in the ECS, approximately 80 km from Shanghai. Although local anthropogenic emissions were negligible there, this island was frequently affected by terrestrial transport during winter and spring, when prevailing

northwesterly winds dominated (Fu et al., 2018; Qin et al., 2016). A cruise campaign was conducted aboard the research vessel (R/V) Dongfanghong III. The cruise routes, as shown in Figure 1a, covered most of the YS and ECS regions. Land-based measurements were conducted at a super site (Dianshan Lake, DSL) in the rural Shanghai Qingpu District. This super site is located at the intersection of Shanghai, Zhejiang, and Jiangsu provinces.



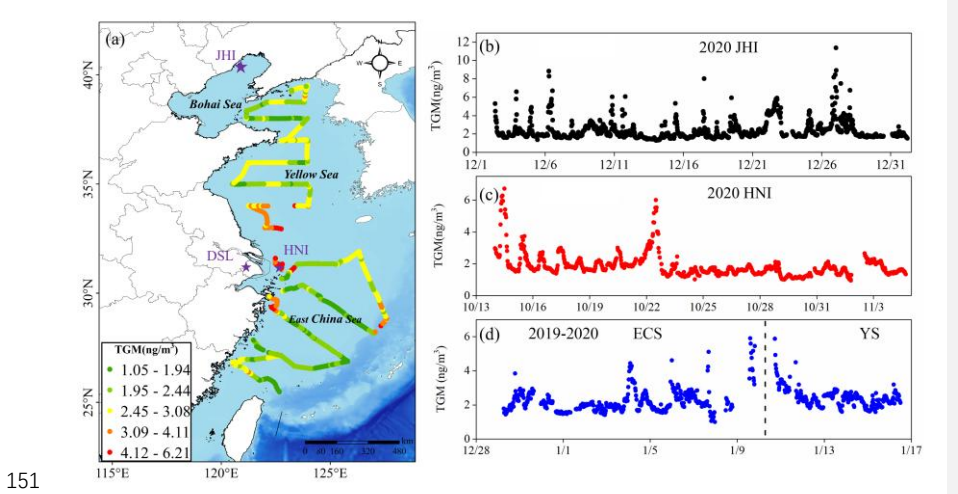


**Figure 1.** (a) The locations of two island sites (JHI and HNI) and one inland site (DSL) denoted by purple pentagrams. The spatial distribution of TGM concentrations over the East China Sea (ECS) and the Yellow Sea (YS) is shown along the cruise routes. The time series of TGM concentrations are measured at (b) JHI, (c) HNI, and (d) ECS+YS, respectively.

## 2.2 TGM/GEM measurements

TGM measurements were performed utilizing a modified Tekran 2600 instrument across various locations and timeframes, i.e., JHI from December 2, 2020 to January 1, 2021, HNI from October 14 to November 4, 2020, and aboard the research vessel (R/V) Dongfanghong III from December 29, 2019 to January 16, 2020. The Tekran 2600 monitor operated similarly to Tekran 2537B, which is widely used for continuous collection and analysis of atmospheric mercury (Sprovieri et al., 2016; Landis and Keeler, 2002). During the operation of the modified Tekran 2600, atmospheric mercury was adsorbed onto the first gold trap over a 24-minute sampling period. After

sampling, the mercury on the first gold trap was thermally desorbed and transferred to the second gold trap. The second trap was then analyzed by the detector during a 6-minute detection phase, resulting in an overall 30-minute sample resolution. To ensure data quality during cruise observations, the instrument was calibrated daily using the external calibration unit Tekran 2505. Samples were pre-dried via a soda lime drying tube prior to detector entry to prevent humidity interference. Additionally, the drying tube and Teflon filter underwent replacement bi-weekly to maintain optimal performance.

GEM measurements were conducted at DSL in Shanghai from October to December, 2020, employing the atmospheric mercury monitoring system (Tekran 2537B/1130/1135) as documented in our prior study (Qin et al., 2020). Briefly, GEM was captured utilizing dual gold cartridges at a flow rate of 1.0 LPM and 5-minute intervals. Subsequently, GEM underwent thermal decomposition for detection via CVAFS. During the sampling process, rigorous quality controls were applied. Prior to sampling, denuders and quartz filters were duly prepared and cleansed adhered to Tekran technical directives. To ensure accuracy, calibration was routinely executed every 47 hours using an internal permeation source, alongside manual injections of standard saturated mercury vapor. For the Tekran 2537B, the average duplication rate between the A and B traps is 99%, with deviations between the two traps consistently below 3%. To mitigate the impact of high humidity on the instrument, samples are first passed through a soda lime drying tube for dehumidification before entering the detector. Further, the KCl-coated denuder, Teflon-coated glass inlet, and impactor plate were swapped weekly, while the quartz filters underwent monthly replacement.

It is noteworthy that TGM in the atmosphere comprises GEM and GOM (gaseous oxidized mercury). Generally, GEM constitutes over 95% of atmospheric mercury (Mao et al., 2016), particularly in the marine boundary layer, including China's marginal seas (Wang et al., 2016b; Fu et al., 2018; Ci et al., 2011; Wang et al., 2019a). Therefore, this study does not differentiate between TGM and GEM, conforming to analogous treatments in existing research (Fu et al., 2018; Ci et al., 2011).

#### 2.3 DGM measurement

DGM (dissolved gaseous mercury) collection from seawater adhered to the procedure

described in previous studies (Gardfeldt et al., 2003; O'driscoll et al., 2003). The sampling process involved the following steps. 1.5 L of surface seawater was collected in a Teflon bottle and subsequently transferred into a borosilicate glass bottle. An introduction of free-Hg argon at approximately 500 ml/min purged the seawater for 60 minutes to extract the DGM onto a gold trap, aided by a soda lime tube deployed to extract water vapor prior to the gold trap. The gold trap was maintained at  $\sim$ 50°C during extraction to prevent water vapor condensation. The DGM stored in the gold trap was measured using the Tekran 2600 post-sampling. To assure quality, stringent assurance and control measures were enacted through replicated field blank experiments. DGM excised from an equivalent volume of Milli-Q water served as the analytical system blank, encompassing a total of 12 blank experiments during field samplings at JHI and HNI, as well as during the R/V measurements. The mean system blank calculated was  $2.5\pm1.3$  pg/L (n = 20), with a detection limit of 3.4 pg/L.

### 2.4 Ancillary data

At JHI, water-soluble ions in  $PM_{2.5}$ , including sulphate ( $SO_4^{2-}$ ), nitrate ( $NO_3^{-}$ ), ammonium ( $NH_4^+$ ), chloride ( $CI^-$ ), sodium ( $Na^+$ ), potassium ( $K^+$ ), magnesium ( $Mg^{2+}$ ), calcium ( $Ca^{2+}$ ), alongside the soluble gases such as ammonia ( $NH_3$ ) and sulfur dioxide ( $SO_2$ ) were continuously monitored using an In-situ Gas and Aerosol Composition monitoring system (IGAC) (Wang et al., 2022). IGAC operated at a 1-hour temporal resolution and consisted of a wet annular denuder (WAD) and ion chromatography (IC) equipped with columns CS17 and CG17 for cations and AG11-HC and AS11-HC for anions. Ambient air was drawn into a  $PM_{2.5}$  cyclone inlet by a built-in pump at a flow rate of 16.7 L/min. The sampled air was separated by passing through the vertically placed WAD to capture water-soluble gases, and airborne particles were collected by a steam scrubber and impact aerosol collector placed downstream. Air samples were dissolved by 30 ml ultra-pure water (18.25  $M\Omega$  cm<sup>-1</sup>) and then divided into two steams. Both aqueous samples (including particles and gases) were injected into the IC system by two separated syringe pumps for analyzing the cations and anions. For quality assurance/quality control (QA/QC) of IGAC, a standardized lithium bromide (LiBr) solution was continuously introduced into aerosol liquid samples during the campaign to validate sampling and analytical stability. Weekly calibrations were performed for the ion

chromatography (IC) module using certified standard solutions, with linearity (R<sup>2</sup> > 0.99) and detection limits (LODs) validated. Black carbon (BC) in PM<sub>2.5</sub> was measured continuously using a multi-wavelength Aethalometer (AE-33, Magee Scientific, USA). Meteorological parameters were measured using a Vaisala WXT530 surface weather station (Vaisala, Finland). Surface seawater temperature was recorded by a YSI EC300 portable conductivity meter (YSI, USA) with a resolution of 0.1°C.

At HNI, methods for analyzing meteorological parameters, BC, and surface seawater temperature mirrored those employed at JHI.

During the cruise campaign, the meteorological metrics (e.g., air temperature, wind speed/direction) and surface seawater temperature were collected from the Finnish Vaisala AWS430 shipborne weather station onboard the R/V. AE-33 was also used for BC measurements during the cruise.

At DSL, water-soluble ions in PM<sub>2.5</sub> and soluble gases were also measured by the IGAC instrument. Trace metals in PM<sub>2.5</sub> (Al, Ti, V, Cr, Mn, Fe, Co, Ni, Cu, Zn, Ga, As, Sr, Cd, Sn, Sb, Ba, Tl, Pb, and Bi) were continuously measured using an Xact multi-metals monitor (Model Xact<sup>TM</sup> 625, Cooper Environmental Services LLT, OR, USA). It operated at a flow rate of 16.7 L min<sup>-1</sup> with hourly resolution. Particles in the airflow passed through a PM2.5 cyclone inlet and were deposited onto a Teflon filter tape, then the samples were transported into a spectrometer for analysis via nondestructive energy-dispersive X-ray fluorescence.

Planetary boundary layer (PBL) height data were obtained from the Global Data Assimilation System (GDAS) archive maintained by the U.S. National Oceanic and Atmospheric Administration (NOAA), available through the READY (Real-time Environmental Applications and Display sYstem) portal (<a href="https://www.ready.noaa.gov/archives.php">https://www.ready.noaa.gov/archives.php</a>; last accessed: 11 May 2025). The dataset, featuring 1-hour temporal resolution, was processed and extracted using MATLAB R2021b (MathWorks, Natick, MA).

#### 250 2.5 Positive matrix factorization (PMF)

The PMF model is recognized for its efficacy in elucidating sources profiles and quantifying

source contributions (Paatero and Tapper, 1994). The underlying principle of PMF posits that sample concentration is dictated by source profiles with disparate contributions, mathematically represented as:

$$X_{ij} = \sum_{k=1}^{P} g_{ik} f_{kj} + e_{ij}$$
 (1)

where Xij represents the concentration of the jth species in the ith sample,  $g_{ik}$  is the contribution of the kth factor in the ith sample,  $f_{kj}$  provides the information about the mass fraction of the jth species in the kth factor,  $e_{ij}$  is the residual for specific measurement, and P represents the number of factors.

The objective function, defined in Eq. (2) below, represents the sum of the squared differences between measured and modeled concentrations, weighted by concentration uncertainties. Minimizing this function allows the PMF model to determine optimal non-negative factor profiles and contributions:

263 
$$Q = \sum_{i=1}^{n} \sum_{j=1}^{m} \left( \frac{x_{ij} - \sum_{k=1}^{p} A_{ik} F_{kj}}{S_{kj}} \right)^{2}$$
 (2)

Where  $X_{ij}$  denotes the concentration of the  $j^{th}$  pollutant in the  $i^{th}$  sample,  $A_{ik}$  represents the contribution of the  $k^{th}$  factor to the  $i^{th}$  sample,  $F_{kj}$  is the mass fraction of the  $j^{th}$  pollutant in the  $j^{th}$  pollutant in  $k^{th}$  factor,  $S_{ij}$  is the uncertainty of the  $j^{th}$  pollutant in the  $i^{th}$  sample, and p is the number of factors. Detail description can be seen in the previous study (Paatero and Tapper, 1994).

TGM, air temperature (unit: Kelvin), gaseous pollutants, and major aerosol chemical species were used as inputs for the PMF model. We tested factor numbers ranging from 3 to 8, with the optimal solution determined by analyzing the slope of the Q-value versus factor count. Model stability was assessed through residual analysis, correlation coefficients between observed and predicted concentrations, and Q-value trends. A six-factor solution in DSL and a five-factor solution at JHI provided the most stable and interpretable results.

At DSL, we selected observational data from October to December, 2020 (totaling 1,080 valid data points) for PMF modeling to align with the HNI observational campaign. At JHI, observational data from December 2 to 30, 2020 (totaling 675 valid data points) were used for PMF analysis.

# 2.6 Sea-air exchange flux

The sea-air exchange fluxes of Hg<sup>0</sup> were calculated via the following equation (Andersson et al., 2008a; Wanninkhof and Oceans, 1992; Wangberg et al., 2001):

281  $F = K_W(C_W - C_a/H')$  (3)

where F is the sea-air exchange flux, K<sub>w</sub> represents the gas exchange velocity, C<sub>w</sub> and C<sub>a</sub> represent the DGM concentration in seawater and the TGM concentration in the atmosphere, respectively, H' is the dimensionless Henry's law coefficient of Hg<sup>0</sup> between the atmosphere and seawater. K<sub>w</sub> is

calculated as follows (Soerensen et al., 2010b; Nightingale et al., 2000).

286 
$$K_w = 0.31u_{10}^2 (S_{C_{Hg}}/660)^{-0.5}$$
 (4)

where  $u_{10}$  is 10-meter wind speed,  $S_{C_{Hg}}$  is the Schmidt number of  $Hg^0$ , 660 is the Schmidt number

 $288 \qquad of \ CO_2 \ in \ 20 \ ^{\circ}\! C \quad seawater \ (Poissant \ et \ al., 2000). \ The \ Schmidt \ number \ for \ Hg \ (S_{CHg}) \ was \ calculated$ 

289 as:

$$S_{C_{Hg}} = v/D_{Hg}$$
 (5)

where v is seawater kinematic viscosity (Wanninkhof, 2014) and  $D_{Hg}$  is the diffusion coefficient of

292 Hg (Kuss et al., 2009).

293 H' is calculated as follows (Andersson et al., 2008a).

294 
$$H' = \exp(-2403.3/T + 6.92)$$
 (6)

Where T is the surface seawater temperature in K.

295296297

298

299

300

301 302

303

304

305

306

307

308

## 3. Results and Discussions

## 3.1 Characteristics of TGM over Chinese marginal seas

Figure 1b-d shows the time series of TGM concentrations measured during three field campaigns, including December 2, 2020 to January 1, 2021 at Juehua Island (JHI), October 14, 2020 to November 4, 2020 at Huaniao Island (HNI), and December 29, 2019 to January 16, 2020 over the Yellow Sea and East China Sea (YS/ECS). The mean TGM concentrations during the three periods were  $2.32 \pm 1.02$  ng/m³,  $1.85 \pm 0.74$  ng/m³, and  $2.25 \pm 0.66$  ng/m³, respectively. TGM at JHI exhibited pronounced fluctuations, frequently surpassing high values of 6 ng/m³, which was attributed to the enhanced coal combustion for residential heating in winter (Li et al., 2023). Conversely, TGM at HNI and across the YS/ECS demonstrated less fluctuations, with concentrations predominantly remaining below 6 ng/m³. The cruise campaign unveiled the spatial distribution of TGM over the ocean (Figure 1a), generally showing its decreasing trend with the

increased distance away from the continent. Specifically, hot spots were observed in the eastern oceanic region of Jiangsu province, the Changjiang estuary, and the outer sea close to the Hangzhou Bay. The continental outflows likely explained this phenomenon. The mean TGM concentrations reached  $2.36 \pm 0.65$  ng/m³ and  $2.16 \pm 0.81$  ng/m³ over the Yellow Sea and East China Sea, respectively, significantly higher than the background level in the Northern Hemisphere  $(1.58 \pm 0.31$  ng/m³) (Bencardino et al., 2024) and also surpassing measurements recorded in the other open ocean areas such as the South China Sea  $(1.52\pm0.32$  ng/m³), Mediterranean Sea  $(1.8\pm1.0$  ng/m³), Bering Sea  $(1.1\pm0.3$  ng/m³), Pacific Ocean (1.15-1.32ng/m³), and Atlantic Ocean  $(1.63\pm0.08$  ng/m³) (Laurier and Mason, 2007; Soerensen et al., 2010a; Mastromonaco et al., 2017; Kalinchuk et al., 2018; Wang et al., 2019b). 72h air mass backward trajectory analyses revealed that air masses over the YS predominantly originated from Liaoning and Inner Mongolia province in northern China, whereas trajectories over the ECS were largely dispersed across the ocean and Eastern China (Figure S1). This divergence may be one of the reasons why the TGM concentration in the YS was higher than that in the ECS.

The diurnal variations of TGM concentrations along with ambient temperature and sun flux during the three periods are displayed in Figure 2. At HNI, TGM commenced increasing at 7:00 a.m., peaking at around 2.44 ng/m³ by 12:00, subsequently declining and stabilizing post 6:00 p.m. The mean TGM concentration during daytime (06:00-18:00) (2.00 ± 0.80 ng/m³) surpassed that of nighttime (1.66 ± 0.40 ng/m³) (t test, p < 0.001). The TGM diurnal pattern displayed strong concordance with temperature and solar flux (Figure 2a), indicative of significant impacts from natural sources (Osterwalder et al., 2021; Huang and Zhang, 2021; Mason et al., 2001). At JHI (Figure 2b), TGM also rose around early morning and peaked at 2.65 ng/m³ by 10:00 a.m., with nocturnal levels markedly increasing from 2.12 ng/m³ at 6:00 p.m. to 2.60 ng/m³ at 11:00 p.m. During daytime, TGM generally showed consistent variation with temperature and sun flux, indicating the influence of natural mercury release. However, the notable frequency of nocturnal peaks suggested that in addition to natural sources, TGM measured at JHI was also significantly affected by anthropogenic sources and unfavorable atmospheric diffusion conditions, specifically from coal combustion for the winter residential heating in northern China (Li et al., 2023). The diurnal pattern of TGM throughout the cruise campaign diverged from those of HNI and JHI,

lacking a consistent relationship with temperature and sun flux. This was mainly due to that the cruise sampling was variable in both the temporal and spatial scale.

339340

338

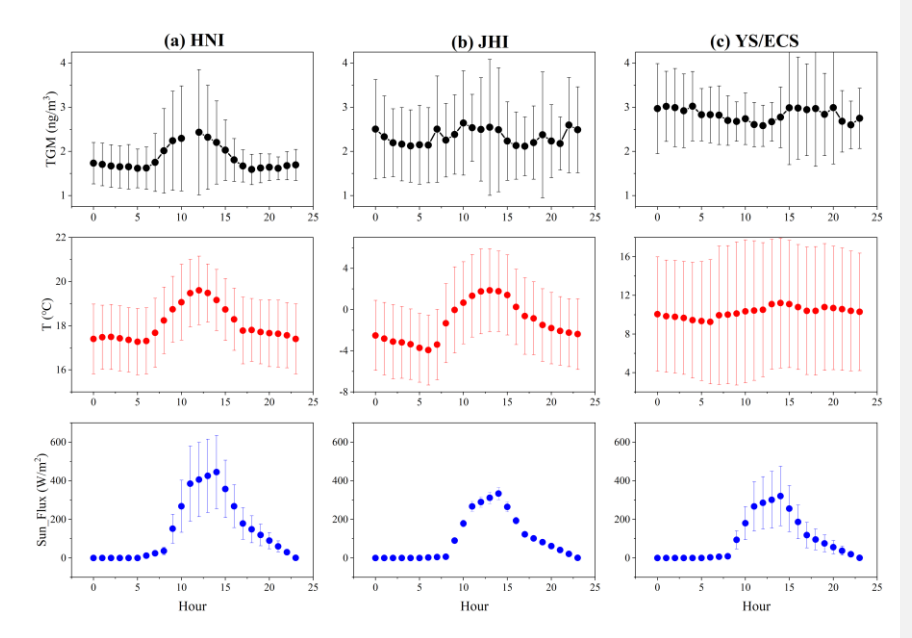


**Figure 2.** Diurnal variations of TGM, ambient temperature and sun flux at (a) HNI, (b) JHI, and (c) the YS/ECS cruise, respectively.

343344

345

346347

348349

354

355

341342

Positive correlations between TGM concentrations and ambient temperature at both HNI and JHI were observed, yielding R<sup>2</sup> values of 0.53 and 0.60, respectively (Figure 3a&3b). Since temperature played a crucial role in Hg<sup>0</sup> release from natural surfaces (Lindberg et al., 1998; Poissant et al., 2000), the evident correlation between TGM and temperature exemplified the significant effects of natural surface emissions.

Positive correlations were also observed between TGM, relative humidity, and wind speed at both HNI and JHI (Figure 3). The positive correlation between humidity and TGM may be due to the fact that high humidity is typically associated with the stable atmospheric stratification, which promoted the accumulation of TGM. As for wind speed, it is a key parameter influencing air-sea

exchange in the double-membrane theory model Wanninkhof, 1992, For example, Soerensen et

al. (2014) found a 2-4 times greater Hg<sup>0</sup> flux due to the high wind speed in the Intertropical

Formatted: Font: 10.5 pt

Formatted: Font: 10.5 pt

Formatted: Font: 10.5 pt

Convergence Zone (ITCZ) region. Previous studies suggested wetting processes may promote the reduction of Hg<sup>#</sup> to Hg<sup>0</sup> in surface seawater, while higher wind speed accelerated its evasion (Lin et al., 2010; Soerensen et al., 2013). This may explain the observed positive correlations between humidity, wind speed, and TGM concentrations.

356

357

358

359

360

361 362

363

364

365

366 367

368

369 370

371

372

373

374

375

376

At HNI, TGM increased concurrently with rising Planetary Boundary Layer (PBL) heights from around 380 to 1000 m, yet decreased with further increase in PBL beyond around 1000 m (Figure 3a). This observed diurnal pattern of TGM may primarily stem from the interplay between temperature-driven natural surface emissions and atmospheric dilution effects. When the PBL height was below 1 km, its increase coincided with rising temperature. Under these conditions, the enhancement of natural surface emissions due to temperature outweighed the dilution effect caused by the developed PBL, leading to increased TGM concentrations. Afterwards, as the PBL height continued to rise, the dilution effect gradually surpassed the temperature-driven emission enhancement, resulting in a decline of TGM concentrations. In contrast, the similar phenomenon lacked manifestation at JHI, where TGM concentrations decreased with the increase of PBL (Figure 3b). Due to the significantly lower marine mercury emissions in the BS (Wang et al., 2020) than in the ECS (Wang et al., 2016a), this phenomenon was likely ascribed to that the natural release around JHI was weaker than that around HNI, thus the dilution effect of elevated PBL overwhelmed the effect of natural surface emissions. Compared to HNI and JHI, the cruise campaign showed almost no relationship between TGM and temperature, relative humidity, wind speed, or PBL height were identified (Figure 3c), which shared similar reasons as discussed in the diurnal variation of TGM.

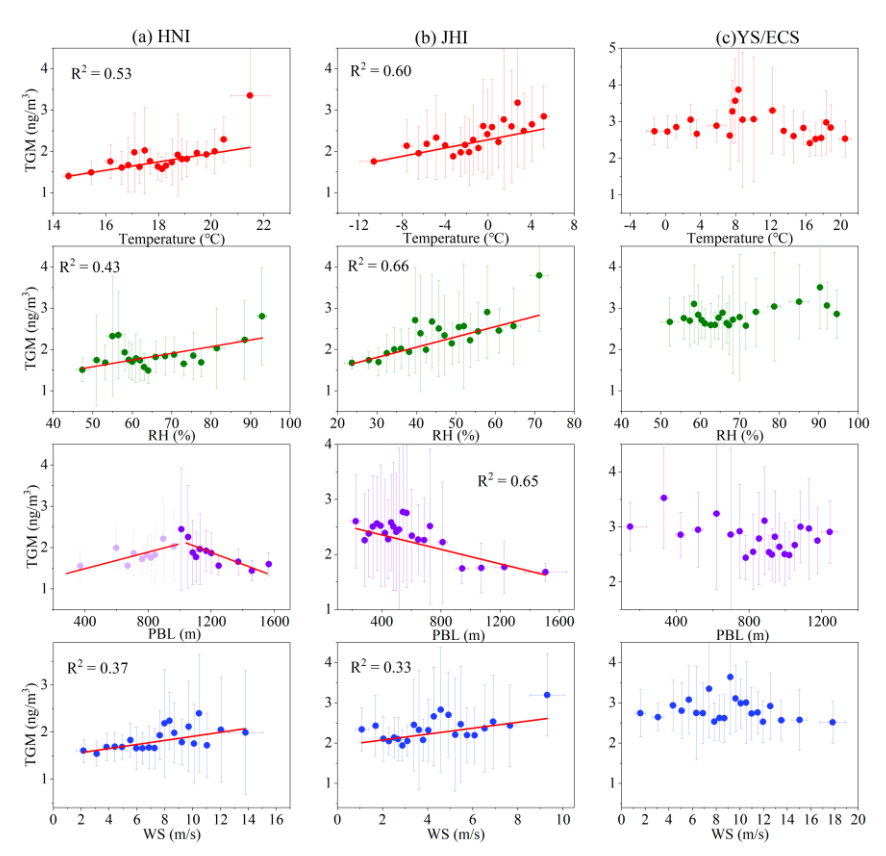


**Figure 3.** Relationship between TGM concentration and temperature, relative humidity, planetary boundary layer height, and wind speed at (a) HNI, (b) JHI, and (c)YS/ECS, respectively.

# 3.2 Influence of continental outflows on marine TGM

The potential source regions of TGM at HNI and JHI are illustrated in Figure S2. At HNI, TGM mainly derived from the lands of Jiangsu Province and vast coastal waters of the East China Sea. While at JHI, the hot spots of TGM were mainly located in the southern Mongolia and Beijing-Tianjin-Hebei regions. This indicated that the relatively high TGM concentrations at the coastal islands were closely related to the continental outflows. Using HNI as an example, Figure S3 compares the daily mean TGM concentration at HNI with the daily mean concentrations of CO, SO<sub>2</sub>, and PM<sub>2.5</sub> in nearby coastal cities including Zhoushan, Ningbo, Jiaxing, Shanghai, and Ningbo. Consistently temporal variations were observed between TGM and these pollutants, particularly for

the peak concentrations, further confirming that offshore TGM concentrations were significantly influenced by continental outflows.

390

391

392

393

394

395 396

397

398

399

400

401

402

403

404

405

406

407

408

409

410

411

412

413

414

415

416

417

418

To assess the impact of anthropogenic sources on marine TGM, the daily TGM concentrations at HNI and DSL (a suburban site in the Yangtze River Delta, Figure 1a) were compared (Figure 4a). Their concentration time series exhibited moderate agreement, suggesting potential land-sea interactions. Furthermore, the correlation between TGM and BC at DSL was pronounced (R<sup>2</sup>=0.56, Figure 4b). This was expected, as BC primarily originated from fossil fuels combustion (Li et al., 2021; Briggs and Long, 2016), which was also the major anthropogenic source of TGM (Pacyna et al., 2006; Streets et al., 2011; Liu et al., 2019). In contrast, the correlation between TGM and BC at HNI was much weaker (R<sup>2</sup>=0.34, Figure 4c). Being an offshore site, HNI could be more strongly influenced by natural sources than DSL.

To qualitatively evaluate the relative importance of anthropogenic and natural sources to TGM, the ratio of TGM/BC was introduced as a qualitative index. an indicator with lower ratios implying the prevalence of anthropogenic sources, and vice versa. Since TGM and BC shared common anthropogenic sources, and TGM had additional natural sources, an increase in the TGM/BC ratio may indicate the growing importance of natural source contributions, and vice versa. Figure 4d shows that the TGM/BC ratio at DSL (mean of 1.6 ng  $\mu g^{\text{-}1}$ ) was substantially lower than that at HNI (5.2 ng µg<sup>-1</sup>). On one hand, lower contribution of anthropogenic sources to TGM in the coastal environment compared to the urban environment was expected. On the other hand, BC deposited more quickly than TGM, thus also elevating the TGM/BC ratios was at locations far from emission sources. The cruise measurement illustrated the spatial distribution of the TGM/BC ratio over YS/ECS (Figure 4e), showing a tendency of decreasing values with increasing distance away from the coasts (Figure 4e). In the East China Sea, the TGM/BC ratio increased with increasing distances away from the coasts. For instance, in the East China Sea, the TGM/BC ratio near the coasts typically ranged from 0.3 to 5.2 ng  $\mu g^{-1}$ , while offshore values generally fluctuated between 8.6 and 22.9 ng µg<sup>-1</sup>. This indicated the contribution of natural sources to TGM obviously increased over the open ocean waters. However, this spatial trend was not observed in the Yellow Sea. As depicted in Figure 4e, the very northern, western, and eastern cruise legs in the Yellow Sea showed relatively low TGM/BC ratios compared to the other cruise periods. This phenomenon should be due to the

Formatted: Font: (Asian) + Body Asian (等线), 10.5 pt, Font color: Auto

Formatted: Font: (Asian) + Body Asian (等线), 10.5 pt,

Formatted: Font: (Asian) + Body Asian (等线), 10.5 pt,

Font color: Auto

Formatted: Font: 10.5 pt, Font color: Auto

Formatted: Font: (Asian) + Body Asian (等线), 10.5 pt, Font color: Auto

Formatted: Font: 10.5 pt, Font color: Auto

Formatted: Font: (Asian) +Body Asian (等线), 10.5 pt,

Font color: Auto

Formatted: Font: 10.5 pt. Font color: Auto

Formatted: Font: (Asian) + Body Asian (等线), 10.5 pt,

Font color: Auto

Yellow Sea being a comparatively enclosed basin, as these cruise legs above were geographically close to Liaoning province in northeast China, the North China Plain, and the Korean Peninsula. Thus, more influences from the terrestrial emissions induced the low TGM/BC ratios. This further corroborated the important contribution of marine natural emissions to TGM. In regard of different maritime-spaces, the northern oceanic regions showed considerably lower values than those in the southern sea regions. In the Yellow Sea, the mean TGM/BC ratio was 4.1 ng μg<sup>-1</sup>, noticeably lower than that of 6.5 ng μg<sup>-1</sup> observed in the East China Sea.

Formatted: Font: (Asian) +Body Asian (等线), 10.5 pt,

**Formatted:** Font: (Asian) +Body Asian (等线), 10.5 pt, Font color: Auto

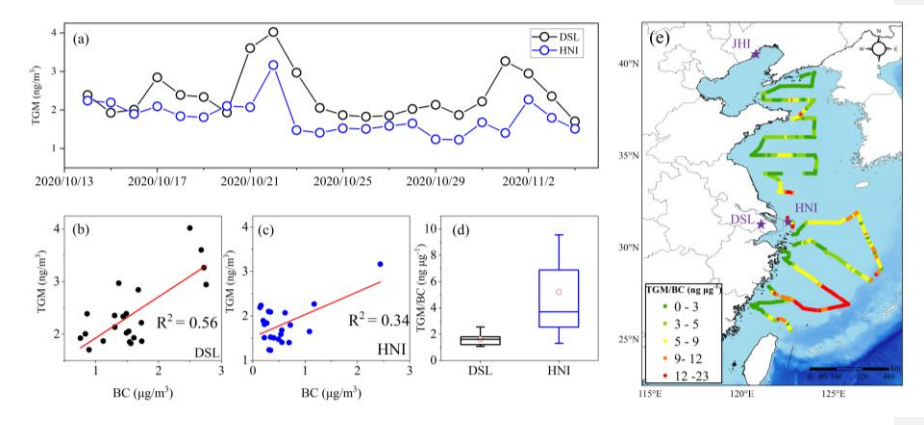


**Figure 4.** (a) Comparison of the daily TGM concentrations between DSL and HNI; Correlation between TGM and BC at (b) DSL and (c) HNI; (d) Comparison of the TGM/BC ratio between DSL and HNI; (e) Spatial distribution of the TGM/BC ratio along the cruise routes over the ECS and YS.

### 3.3 Quantification of anthropogenic vs. marine sources to TGM

Based on the discussions above, it is essential to disentangle the anthropogenic and natural sources of atmospheric mercury. Here, the PMF model was employed for the comprehensive dataset obtained at DSL and JHI, respectively. Considering the direct correlation between temperature and natural release of atmospheric mercury (Wang et al., 2014; Zhu et al., 2016) and the indirect correlation between ammonia and natural release of atmospheric mercury (Qin et al., 2019), we utilized temperature and ammonia as indicators of natural atmospheric mercury sources, which has been proven feasible (Qin et al., 2020). Inputs for PMF also encompassed SO<sub>4</sub><sup>2-</sup>, Cl<sup>-</sup>, NO<sub>3</sub><sup>-</sup>, Na<sup>+</sup>,

NH<sub>4</sub><sup>+</sup>, K<sup>+</sup>, Mg<sup>2+</sup>, Ca<sup>2+</sup>, SO<sub>2</sub>, NO, Pb, Fe, K, Cr, Se, Ca, V, Mn, As, and Ni. While running the PMF model, we tested the number of factors from three to eight and determined the optimal solutions through analyzing the slope of the Q values in relation to the number of factors. The analyses revealed that a six-factor solution for DSL and a five-factor solution for JHI produced the most robust and coherent interpretations.

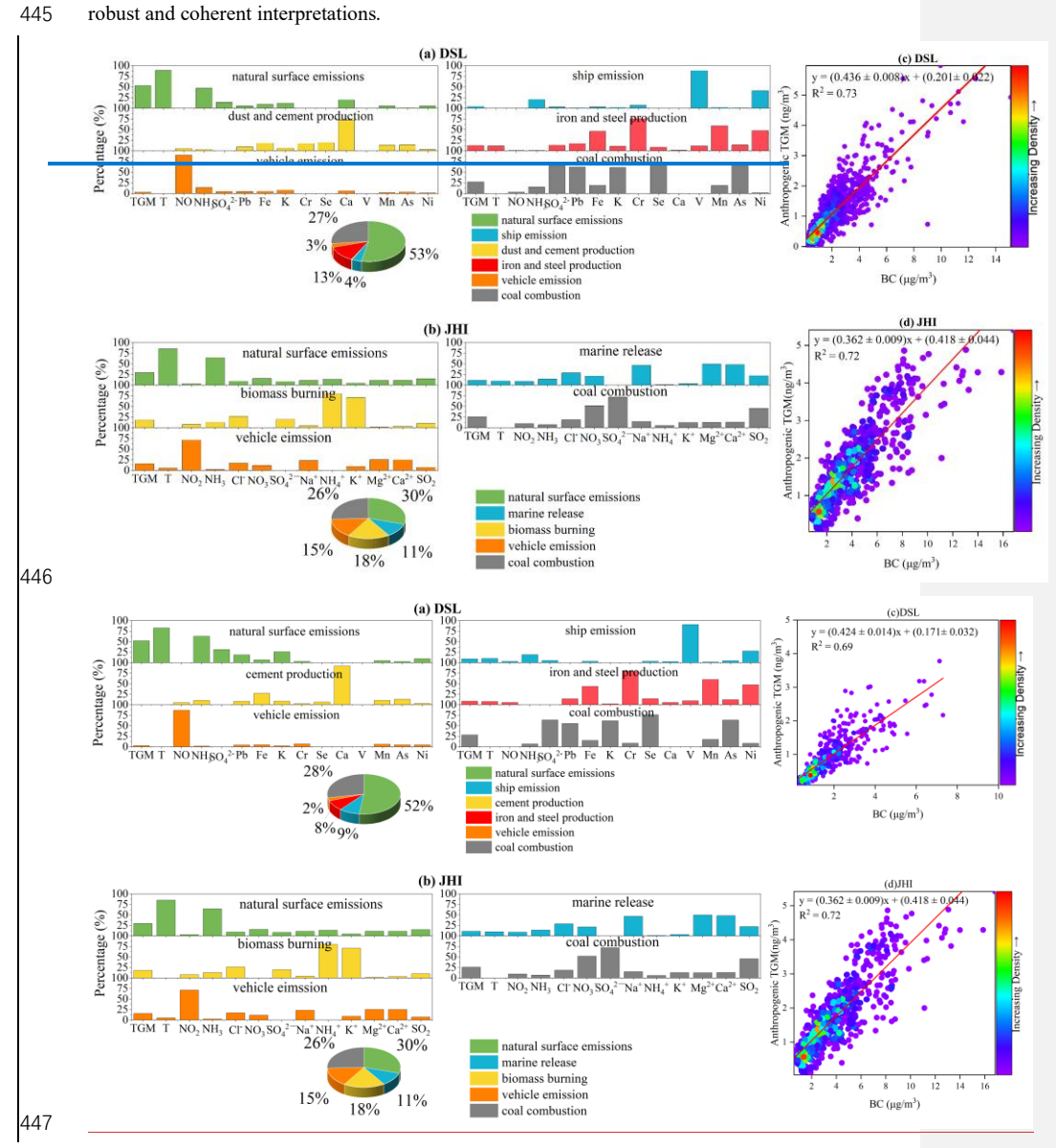


**Figure 5.** Source apportionment of TGM at (a) DSL and (b) JHI; Linear relationship between BC and anthropogenic TGM at (c) DSL and (d) JHI.

449450451

452

453

454

455

456

457 458

459

460

461

462 463

464

465

466

467

468

469

470

471

472

473

474

475

476

448

As detailed in Figure 5a, six distinct factors were resolved by PMF at DSL. The factor characterized by high loadings of temperature, NH<sub>3</sub>, and TGM represented the natural surface emissions of mercury. A second factor with notable loading of V and moderate loading of Ni was ascribed to be shipping emissions, as V has been considered a typical tracer of heavy-oil combustion, which is commonly used in marine vessels (Viana et al., 2009). The dust and cement production was associated with a factor exhibiting prominent Ca loading. The factor displaying high loading of Cr and moderate loadings of Fe and Mn was attributed to iron and steel production. Another factor, categorized by elevated NO levels, was linked to vehicle emissions. Finally, the factor with high loadings of SO<sub>4</sub><sup>2</sup>-. Pb, K, Se, and As was indicative of coal combustion. PMF results indicated that the contributions of anthropogenic and natural sources to TGM were approximate 48% and 52% at DSL, respectively. By applying the same PMF modeling strategy at JHI, the contributions of anthropogenic and natural sources to TGM at JHI were 59% and 41%, respectively (Figure 5b). The source apportionment results signified substantial influences of both human and natural factors on TGM levels, with their contributions being nearly equivalent. Furthermore, correlation analysis was conducted between the absolute contribution of anthropogenic sources to GEM and BC, yielding-a high strong correlations coefficient ( $\mathbb{R}^2$ ) of 0.88 and 0.86 at both DSL (Anthropogenic TGM = (0.424)  $\pm 0.014$ )\*BC + (0.171± 0.032), R<sup>2</sup> = 0.88, Figure 5c) and JHI (Anthropogenic TGM = 0.362 ± 0.009)\*BC +  $(0.431 \pm 0.044)$ ,  $R^2 = 0.86$ , Figure 5dFigure 5e&5d), respectively. It should be noted that BC was not included in PMF modeling, thus the robust relationship between anthropogenic GEM and BC suggested that BC can serve as a viable indicator for quantifying anthropogenic contributions to TGM.

To validate the robustness of this relationship in different years, we derived the relationship between anthropogenic GEM and BC at DSL before 2020 based on the same methodology. It can be found that the regression equation during the winter of previous years was close to that obtained during this study period (Figure S5). In fact, the mercury emissions (Feng et al., 2024) and black carbon emissions (Geng et al., 2024) were quite stable in the neighboring years of this study period.

**Formatted:** Font: (Asian) +Body Asian (等线), 10.5 pt, Font color: Auto

**Formatted:** Font: (Asian) +Body Asian (等线), 10.5 pt, Font color: Auto

Formatted: Font: (Asian) +Body Asian (等线), 10.5 pt, Font color: Auto, Not Highlight

Formatted: Font: (Asian) +Body Asian (等线), 10.5 pt, Font color: Auto

**Formatted:** Font: (Asian) +Body Asian (等线), 10.5 pt, Font color: Auto

**Formatted:** Font: (Asian) +Body Asian (等线), 10.5 pt, Font color: Auto

Formatted: Font: (Asian) +Body Asian (等线), 10.5 pt, Font color: Auto

**Formatted:** Font: (Asian) +Body Asian (等线), 10.5 pt, Font color: Auto

For instance, China's anthropogenic GEM emissions in 2019 and 2020 were 194.2 tonnes and 191.8 tonnes, respectively, showing negligible changes. Thus, it can be assumed that the relationship between anthropogenic GEM and BC remained relatively constant.

Based on the results above, the regression formulas obtained from DSL (Anthropogenie TGM =  $(0.436424 \pm 0.008014)*BC + (0.201171 \pm 0.022032)$ , Figure 5e) and JHI ((Anthropogenie TGM =  $0.362 \pm 0.009)*BC + (0.431 \pm 0.044)$ , Figure 5d) were further applied to the cruise observation for the purpose of differentiating the anthropogenic and natural fractions of TGM over the ocean. The following criteria were applied. If the air mass backward trajectories (purple segments in Figure S54) primarily originated from northern China, the JHI-derived formula was employed; If the air mass backward trajectories (green segments in Figure S54) passed through the Yangtze River Delta region or hovered over the East China Sea, the DSL-derived formula was enacted. Due to the uncertainties of regression slopes and intercepts of the regression formulas, this approach caused around 5% uncertainties on differentiating the anthropogenic and natural fractions of TGM.

Time-series of mass concentrations of anthropogenic and natural TGM in different coastal and oceanic regions after applying the above equations are shown in Figure S<sub>6</sub>5. Concentrations of anthropogenic TGM at HNI, JHI, ECS, and YS were  $0.64 \cdot 61 \pm 0.30 \cdot 29 \text{ ng/m}^3$ ,  $1.28 \pm 0.75 \text{ ng/m}^3$ ,  $0.63 \cdot 59 \pm 0.45 \cdot 41 \text{ ng/m}^3$ , and  $0.92 \pm 0.25 \text{ ng/m}^3$ , respectively. And the concentrations of natural TGM were  $1.45 \cdot 19 \pm 0.46 \cdot 45 \text{ ng/m}^3$ ,  $0.88 \pm 0.26 \text{ ng/m}^3$ ,  $1.54 \cdot 57 \pm 0.52 \cdot 53 \text{ ng/m}^3$ , and  $1.38 \pm 0.51 \text{ ng/m}^3$  at the four locations above, respectively. To ensure the reliability of these results, the relationship between natural TGM and temperature was explored, yielding R<sup>2</sup> of 0.92, 0.76, 0.75, and 0.63 at HNI, JHI, ECS, and YS, respectively (Figure 6). The correlation was significantly stronger than that between the total TGM and temperature, particularly in the ECS and YS regions, where no correlations were observed (Figure 3c). This proved that the quantitative method established above was reliable.

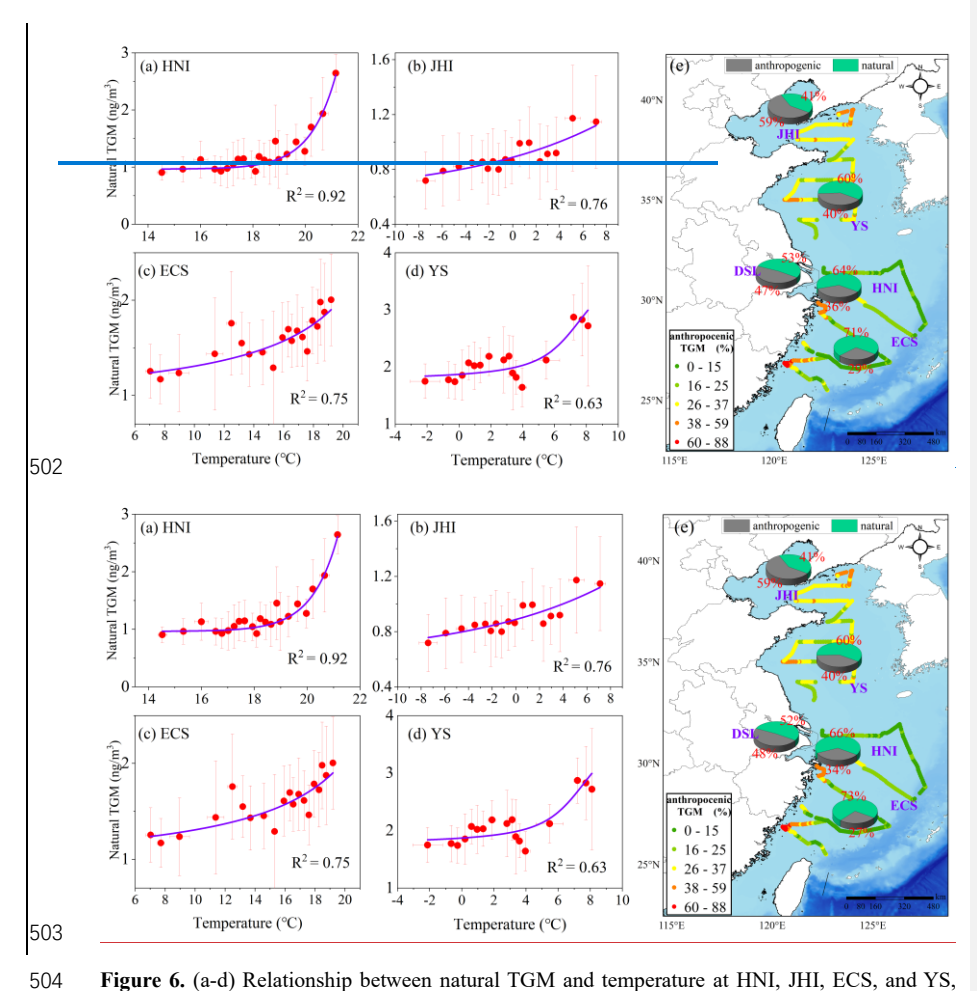


**Figure 6.** (a-d) Relationship between natural TGM and temperature at HNI, JHI, ECS, and YS, respectively. (e) Spatial distribution of the relative contributions of anthropogenic and natural sources to TGM concentrations along the cruise routes. The mean contributions over JHI, HNI, DSL, ECS, and YS are denoted by the pie charts.

The anthropogenic contributions to TGM along the cruise routes are plotted in Figure 6e, demonstrating significantly higher values near the coastal zones compared to the open ocean areas. In details, anthropogenic contributions to TGM near the East China Sea coastal zones reached as high as 60-88%, while the contributions diminished quickly to 15-25% over the open oceans. From the northern oceanic regions to the southern counterparts, the contribution of anthropogenic sources

to TGM generally exhibited a decreasing trend, with values of around 59%, 40%, 3634%, and 2927% over JHI, YS, HNI, and ECS, respectively. In comparison, previous isotope-based source apportionment studies have revealed anthropogenic contributions of 29% and 42% to TGM in remote areas like Changbai Mountain and Ailao Mountain (Wu et al., 2023). In general, the isotopebased results indicated that the relative contributions of anthropogenic emissions to surface GEM in remote China and urban China were around 30% and 49%, respectively (Fu et al., 2021; Feng et al., 2022; Wu et al., 2023). Notably, the anthropogenic contributions to TGM in the Yellow Sea, East China Sea, and Huaniao Island from this study aligned closely with isotope-derived values from China's remote regions, while the DSL findings corresponded with urban isotope results. The elevated contribution observed at JHI (59%) may be attributed to its proximity to the mainland (only 10 km away) and the sampling period occurring during the winter heating season, where continental transport influences were significant (Li et al., 2023). Furthermore, the values obtained in this study fell within comparable ranges to modeling study estimates (typically 33% to 41% on average) (Chen et al., 2014; Wang et al., 2018). As shown in Figure S1, the backward trajectories over the Yellow Sea segment were primarily influenced by air masses from the North China Plain and Liaoning Province. The relatively higher contribution of anthropogenic sources to the Yellow Sea during the cruise was likely attributable to the continental transport from northern China. In addition, during this cruise, the seawater temperature of the Yellow Sea was significantly lower than that of the East China Sea, which was unfavorable for the natural release of mercury.

532533534

535

536

537

538

539

540

541542

514

515

516

517

518

519520

521

522

523

524

525

526

527528

529

530

531

# 3.4 Effects of anthropogenic inputs on the Characteristics of sea-air exchange of mercury in various oceans

To determine the sea-air exchange flux of mercury, DGM (dissolved gaseous mercury) concentrations in seawater were measured at all sampling sites during the cruise (Figure S<u>76</u>). Figure S<u>76</u> delineates the time-series of DGM observed at JHI, YS, HNI, and ECS, with mean concentrations of  $21.3 \pm 4.8$ ,  $29.9 \pm 6.1$ ,  $42.0 \pm 9.4$ , and  $39.7 \pm 10.9$  pg/L, respectively. The DGM concentrations measured during this winter cruise campaign (22.9-39.7 pg/L) were significantly lower than those recorded previously during summer and fall in similar regions (52.4-63.9 pg/L) (Ci et al., 2011; Ci et al., 2015; Wang et al., 2016a), indicating a noticeable seasonal variation in

DGM concentrations in the ECS and YS. This seasonal variation pattern of seawater DGM, with lower levels in winter compared to summer and autumn, can be attributed to the dynamic equilibrium between competing redox processes. This equilibrium can be represented as: Hg2+ + photo-reductants ≠ DGM + photo-oxidants (O'driscoll et al., 2006), During warmer seasons, higher temperature accelerated the volatilization of DGM from seawater, and also drove the equilibrium toward Hg2+ reduction to replenish the lost DGM. Therefore, DGM concentrations in seawater were usually lower in winter due to suppressed redox processes. Spatially, DGM concentrations in the ECS were higher than those in the YS, likely due to the significantly higher sea surface temperature in the ECS (mean: 14.8 °C) compared to the YS (mean: 4.1 °C) during the cruise campaign. Higher temperature not only favored the production of DGM in seawater (Costa and Liss, 1999; Andersson et al., 2011; Mason et al., 2001) but also promoted the escape of DGM from the water surface into the atmosphere (Osterwalder et al., 2021; Huang and Zhang, 2021).. Additionally, we observed that DGM concentrations were higher in coastal waters, particularly near the Yangtze River Estuary, where the concentration reached 51.4 pg/m³. This suggested that continental inputs, such as river discharge, had a significant influence on DGM levels in nearshore waters (Chen et al., 2020; Kuss et al., 2018; Liu et al., 2016).

543

544

545

546

547

548

549

550

551552

553

554

555

556557

558

559560

Formatted: Font: 10.5 pt

Formatted: Font: 10.5 pt

Formatted: Font: 10.5 pt

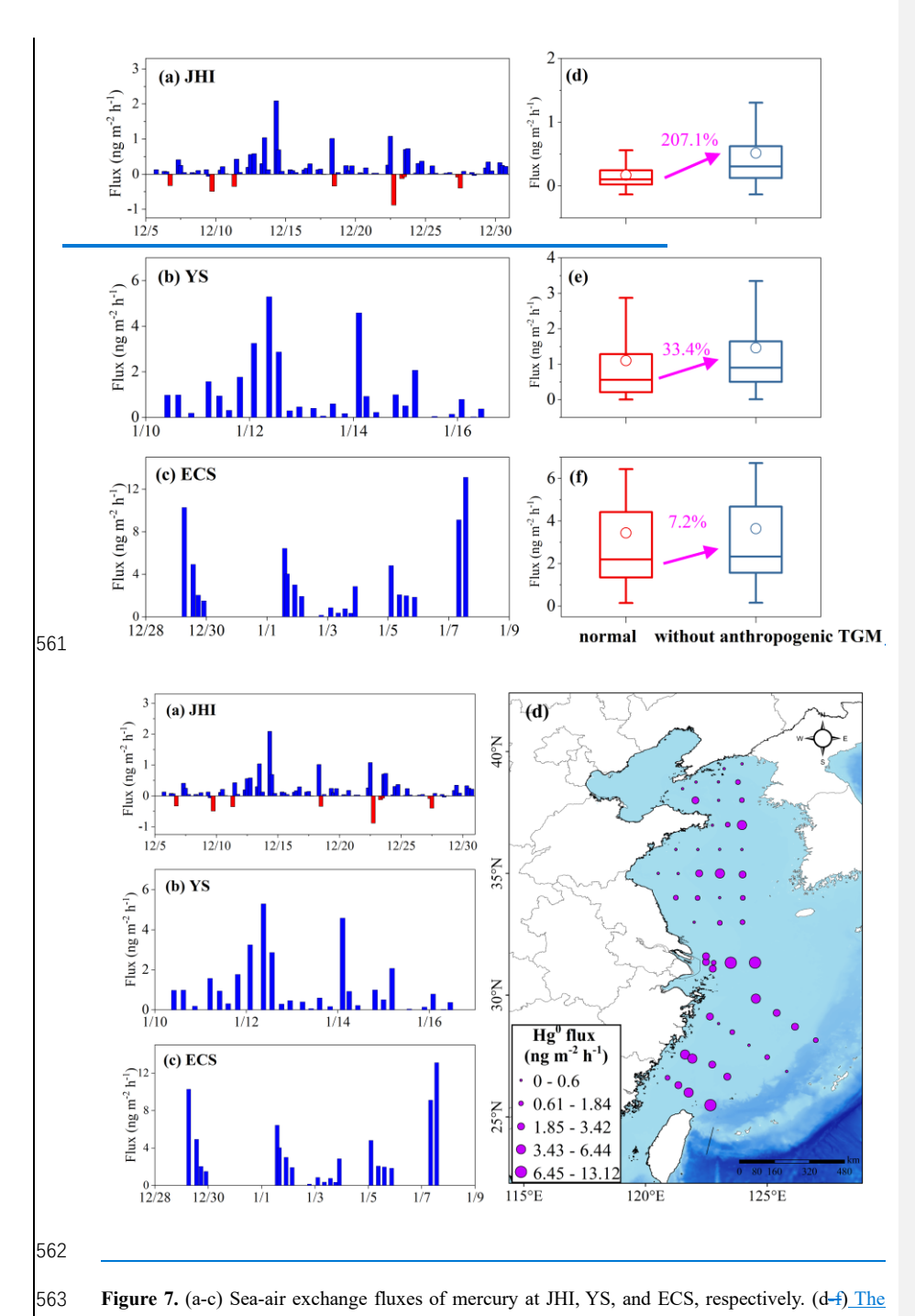


Figure 7. (a-c) Sea-air exchange fluxes of mercury at JHI, YS, and ECS, respectively. (d-f) The

spatial distribution of sea-air exchange flux of —Hg<sup>0</sup> during the cruiseComparison between the normal condition and the "without anthropogenic TGM" scenario, which represented recalculated sea-air exchange fluxes of mercury after subtracting the anthropogenic contributions of TGM concentrations.

Figure 7 shows the time-series and spatial distribution of sea-air exchange fluxes of mercurywithin the BS (represented by JHI), YS, and ECS, which were  $0.17\pm0.38$ ,  $1.10\pm1.34$ , and  $3.44\pm3.24$  ng m<sup>-2</sup> h<sup>-1</sup>, respectively (Table S1). It was evident that the Hg<sup>0</sup> fluxes during winter in the ECS was the highest, followed by the YS and the BS. This finding coincided with the discussions above that natural TGM exhibited much higher concentrations in the ECS and YS than in the BS (Section 3.3). BS acted as a weak mercury source region and even a mercury sink sometimes (negative flux in Figure 7a). Due to the higher concentrations and contributions of anthropogenic TGM in the BS, the release of mercury from the ocean was significantly suppressed, which likely explained the relatively low sea-air exchange flux of mercury there.

Overall, mMercury fluxes observed during winter were lower than previous studies in other seasons, e.g., 4.6±3.6 ng m<sup>-2</sup> h<sup>-1</sup> in ECS during summer (Wang et al., 2016a), 3.07±3.03 ng m<sup>-2</sup> h<sup>-1</sup> in YS during spring (Wang et al., 2020), and 0.59±1.13 ng m<sup>-2</sup> h<sup>-1</sup> in BS during fall (Wang et al., 2020). To assess the impacts of anthropogenic inputs on the sea-air exchange, we recalculated the flux—after—removing—the—anthropogenic—contributions—from—the—TGM—measurements.—This recalculation revealed increases of mercury fluxes in all investigated oceanic regions with different extents. The post-adjustment mercury fluxes in the BS, YS, and ECS increased by 0.347, 0.357, and 0.199 ng m<sup>-2</sup> h<sup>-1</sup>, respectively, corresponding to increased marine mercury emissions of 0.058, 0.308, and 0.332 tons, respectively. Compared to the normal condition, the BS exhibited the most substantial increase in marine mercury release (207.1%) following the deduction of anthropogenic impacts, succeeded by the YS (33.4%) and the ECS (6.5%) (Figure 7d 7f). These results quantitatively elucidated the impact of anthropogenic emissions on marine mercury release, underscoring the potential effects of diminished anthropogenic emissions on oceanic mercury cycling.

Formatted: Superscript

Formatted: Indent: First line: 0.74 cm, Space After: 0 pt, Line spacing: 1.5 lines, No widow/orphan control

**Formatted:** Font: (Asian) +Body Asian (等线), 10.5 pt, Font color: Auto

**Formatted:** Font: (Asian) +Body Asian (等线), 10.5 pt, Font color: Auto

#### 4. Conclusions and implications

This study elucidated the effects of anthropogenic sources on atmospheric mercury concentrations across various marginal seas and the subsequent influence on sea-air exchange dynamics of mercury. Through comprehensive observations across island, cruise, and terrestrial settings, we delineated atmospheric mercury distribution characteristics within the Chinese marginal seas. The relationships between TGM and various environmental parameters suggested the significance of natural sources in constraining oceanic atmospheric mercury levels. Notably, TGM peaks recorded at terrestrial and island sites exemplified the influence of continental outflows on the marine TGM. The introduction of the TGM/BC ratio functioned as a qualitative proxy for assessing the extent of anthropogenic contributions. Furthermore, we articulated a quantitative methodology for assessing anthropogenic contributions to marine atmospheric mercury, revealing that these sources contributed 59%, 40%, and 2927% to atmospheric mercury levels across the Bohai Sea, Yellow Sea, and East China Sea, respectively. The winter sea-air exchange fluxes of mercury in these three seas were estimated as 0.169, 1.100, and 3.442 ng m<sup>-2</sup> h<sup>-1</sup>, respectively, \_-In regions where anthropogenic emissions were intense, sea-air exchange fluxes of mercury were evidently suppressed. with increases of 0.347, 0.357, and 0.199 ng m<sup>2</sup> h<sup>+</sup> subsequent to deducting anthropogenic contributions.

Conducting atmospheric mercury measurements over oceans presented considerable complexities compared to terrestrial observations, further compounded by challenges associated with determining atmospheric mercury sources in the oceanic environment. This study established a quantitative method grounded in extensive observations encompassing terrestrial, island, and marine contexts, facilitating estimations of anthropogenic contributions to atmospheric mercury solely predicated on atmospheric mercury and black carbon data. This methodology may offer valuable insights for analogous analyses of atmospheric mercury and other pollutants across diverse oceanic regions globally. Using this method, we further quantified the extent to which anthropogenic sources suppressed the sea air exchange of mercury. Against the backdrop of declining global anthropogenic atmospheric mercury emissions over the past 30 years, our findings suggested an increase in mercury release from the ocean. Consequently, the mercury content in the ocean will be likely to decrease, resulting in less inorganic mercury available for methylmercury production.

622	These insights contribute to a deeper understanding of the biogeochemical cycle of mercury and
623	enhance our ability to evaluate its impacts on marine ecosystems and human health.
624	
625	Data Availability Statement
626	The raw data generated in this study have been uploaded to Zenodo
627	(https://doi.org/10.5281/zenodo.14847622).
628	
629	Author contributions
630	KH designed this study. XQ, HL, JC, XW, GW, CL, DL, JH, and YL performed data collection.
631	XQ and KH performed data analysis and wrote the paper. All have commented on and reviewed the
632	paper.
633	
634	Competing interests
635	The authors declare that they have no conflict of interest.
636	
637	Acknowledgments
638	This work was financially supported by the National Key R&D Plan Programs
639	(2023YFE0102500, 2018YFC0213105), the National Science Foundation of China (42175119,
640	42361144711), and the Joint Research Fund of the "Island Atmosphere and Ecology" Category IV
641	Peak Discipline (ZD202502). Junjie Wei, Hao Ding, and Qiongzhen Wang acknowledge financial
642	support from Central Guiding Local Science and Technology Development Fund Projects
643	(No.2023ZY1024).
644	
645	References:
646 647 648	Amyot, M., Mierle, G., Lean, D. R. S., and McQueen, D. J.: SUNLIGHT-INDUCED FORMATION OF DISSOLVED GASEOUS MERCURY IN LAKE WATERS, Environmental science & technology, 28, 2366-2371, 10.1021/es00062a022, 1994.
649 650 651	Andersson, M. E., Gårdfeldt, K., Wängberg, I., and Strömberg, D.: Determination of Henry's law constant for elemental mercury, Chemosphere, 73, 587-592, <a href="https://doi.org/10.1016/j.chemosphere.2008.05.067">https://doi.org/10.1016/j.chemosphere.2008.05.067</a> , 2008a.
652	Andersson, M. E., Sommar, J., Gårdfeldt, K., and Jutterström, S.: Air-sea exchange of volatile

- 654 <u>https://doi.org/10.1016/j.marchem.2011.01.005</u>, 2011.
- 655 Andersson, M. E., Sommar, J., Gårdfeldt, K., and Lindqvist, O.: Enhanced concentrations of dissolved
- 656 gaseous mercury in the surface waters of the Arctic Ocean, Mar. Chem., 110, 190-194,
- 657 10.1016/j.marchem.2008.04.002, 2008b.
- 658 Bencardino, M., D'Amore, F., Angot, H., Angiuli, L., Bertrand, Y., Cairns, W., Diéguez, M. C.,
- Dommergue, A., Ebinghaus, R., Esposito, G., Komínková, K., Labuschagne, C., Mannarino, V., Martin,
- 660 L., Martino, M., Neves, L. M., Mashyanov, N., Magand, O., Nelson, P., Norstrom, C., Read, K.,
- 661 Sholupov, S., Skov, H., Tassone, A., Vítková, G., Cinnirella, S., Sprovieri, F., and Pirrone, N.: Patterns
- and trends of atmospheric mercury in the GMOS network: Insights based on a decade of
- 663 measurements, Environmental Pollution, 363, 125104
- 664 https://doi.org/10.1016/j.envpol.2024.125104, 2024.
- Briggs, N. L. and Long, C. M.: Critical review of black carbon and elemental carbon source
- 666 apportionment in Europe and the United States, Atmospheric Environment, 144, 409-427,
- 667 10.1016/j.atmosenv.2016.09.002, 2016.
- 668 Chen, L., Wang, H. H., Liu, J. F., Tong, Y. D., Ou, L. B., Zhang, W., Hu, D., Chen, C., and Wang, X. J.:
- 669 Intercontinental transport and deposition patterns of atmospheric mercury from anthropogenic
- emissions, Atmos. Chem. Phys., 14, 10163-10176, 10.5194/acp-14-10163-2014, 2014.
- 671 Chen, Y.-S., Tseng, C.-M., and Reinfelder, J. R.: Spatiotemporal Variations in Dissolved Elemental
- 672 Mercury in the River-Dominated and Monsoon-Influenced East China Sea: Drivers, Budgets, and
- 673 Implications, Environmental science & technology, 54, 3988-3995, 10.1021/acs.est.9b06092, 2020.
- 674 Ci, Z., Wang, C., Wang, Z., and Zhang, X.: Elemental mercury (Hg(0)) in air and surface waters of
- 675 the Yellow Sea during late spring and late fall 2012: Concentration, spatial-temporal distribution
- and air/sea flux, Chemosphere, 119, 199-208, <a href="https://doi.org/10.1016/j.chemosphere.2014.05.064">https://doi.org/10.1016/j.chemosphere.2014.05.064</a>,
- 677 2015.
- 678 Ci, Z. J., Zhang, X. S., Yin, Y. G., Chen, J. S., and Wang, S. W.: Mercury Redox Chemistry in Waters
- 679 of the Eastern Asian Seas: From Polluted Coast to Clean Open Ocean, Environmental science &
- 680 technology, 50, 2371-2380, 10.1021/acs.est.5b05372, 2016.
- 681 Ci, Z. J., Zhang, X. S., Wang, Z. W., Niu, Z. C., Diao, X. Y., and Wang, S. W.: Distribution and air-sea
- exchange of mercury (Hg) in the Yellow Sea, Atmospheric Chemistry and Physics, 11, 2881-2892,
- 683 10.5194/acp-11-2881-2011, 2011.
- 684 Costa, M. and Liss, P. S.: Photoreduction of mercury in sea water and its possible implications for
- 685 Hg0 air–sea fluxes, Mar. Chem., 68, 87-95, https://doi.org/10.1016/S0304-4203(99)00067-5, 1999.
- Feinberg, A., Selin, N. E., Braban, C. F., Chang, K.-L., Custodio, D., Jaffe, D. A., Kyllonen, K., Landis,
- 687 M. S., Leeson, S. R., Luke, W., Molepo, K. M., Murovec, M., Nerentorp Mastromonaco, M. G., Aspmo
- Pfaffhuber, K., Rudiger, J., Sheu, G.-R., and St Louis, V. L.: Unexpected anthropogenic emission
- 689 decreases explain recent atmospheric mercury concentration declines, Proceedings of the National
- 690 Academy of Sciences of the United States of America, 121, e2401950121,
- 691 10.1073/pnas.2401950121, 2024.
- 692 Feng, X., Li, P., Fu, X., Wang, X., Zhang, H., and Lin, C.-J.: Mercury pollution in China: implications
- on the implementation of the Minamata Convention, Environmental Science: Processes & Impacts,
- 694 24, 634-648, 10.1039/d2em00039c, 2022.
- 695 Fitzgerald, W. F., Lamborg, C. H., and Hammerschmidt, C. R.: Marine Biogeochemical Cycling of
- 696 Mercury, Chemical Reviews, 107, 641-662, 10.1021/cr050353m, 2007.
- 697 Fu, X., Yang, X., Tan, Q., Ming, L., Lin, T., Lin, C.-J., Li, X., and Feng, X.: Isotopic Composition of

- 698 Gaseous Elemental Mercury in the Marine Boundary Layer of East China Sea, Journal of
- 699 Geophysical Research: Atmospheres, 10.1029/2018jd028671, 2018.
- 700 Fu, X., Liu, C., Zhang, H., Xu, Y., Zhang, H., Li, J., Lyu, X., Zhang, G., Guo, H., Wang, X., Zhang, L.,
- 701 and Feng, X.: Isotopic compositions of atmospheric total gaseous mercury in 10 Chinese cities and
- 702 implications for land surface emissions, Atmos. Chem. Phys., 21, 6721-6734, 10.5194/acp-21-
- 703 6721-2021, 2021.
- 704 Fu, X. W., Feng, X. B., Yin, R. S., and Zhang, H.: Diurnal variations of total mercury, reactive mercury,
- 705 and dissolved gaseous mercury concentrations and water/air mercury flux in warm and cold
- seasons from freshwaters of southwestern China, Environ. Toxicol. Chem., 32, 2256-2265,
- 707 10.1002/etc.2323, 2013.
- 708 Fu, X. W., Feng, X. B., Zhang, G., Xu, W. H., Li, X. D., Yao, H., Liang, P., Li, J., Sommar, J., Yin, R. S.,
- 709 and Liu, N.: Mercury in the marine boundary layer and seawater of the South China Sea:
- 710 Concentrations, sea/air flux, and implication for land outflow, J. Geophys. Res.-Atmos., 115, 11,
- 711 10.1029/2009jd012958, 2010.
- 712 Gardfeldt, K., Sommar, J., Ferrara, R., Ceccarini, C., Lanzillotta, E., Munthe, J., Wangberg, I., Lindqvist,
- 713 O., Pirrone, N., Sprovieri, F., Pesenti, E., and Stromberg, D.: Evasion of mercury from coastal and
- 714 open waters of the Atlantic Ocean and the Mediterranean Sea, Atmospheric Environment, 37, S73 -
- 715 S84, 10.1016/s1352-2310(03)00238-3, 2003.
- Horowitz, H. M., Jacob, D. J., Zhang, Y., Dibble, T. S., Slemr, F., Amos, H. M., Schmidt, J. A., Corbitt,
- 717 E. S., Marais, E. A., and Sunderland, E. M.: A new mechanism for atmospheric mercury redox
- 718 chemistry: implications for the global mercury budget, Atmospheric Chemistry and Physics, 17,
- 719 6353-6371, 10.5194/acp-17-6353-2017, 2017.
- 720 Huang, S. and Zhang, Y.: Interannual Variability of Air-Sea Exchange of Mercury in the Global
- 721 Ocean: The "Seesaw Effect" in the Equatorial Pacific and Contributions to the Atmosphere,
- 722 Environmental science & technology, 55, 7145-7156, 10.1021/acs.est.1c00691, 2021.
- 723 Kalinchuk, V. V., Mishukov, V. F., and Astakhov, A. S.: Arctic source for elevated atmospheric
- 724 mercury (Hg-0) in the western Bering Sea in the summer of 2013, Journal of Environmental
- 725 Sciences, 68, 114-121, 10.1016/j.jes.2016.12.022, 2018.
- 726 Kuss, J., Holzmann, J., and Ludwig, R.: An Elemental Mercury Diffusion Coefficient for Natural
- 727 Waters Determined by Molecular Dynamics Simulation, Environmental science & technology, 43,
- 728 3183-3186, 10.1021/es8034889, 2009.
- 729 Kuss, J., Krüger, S., Ruickoldt, J., and Wlost, K. P.: High-resolution measurements of elemental
- 730 mercury in surface water for an improved quantitative understanding of the Baltic Sea as a source
- of atmospheric mercury, Atmos. Chem. Phys., 18, 4361, 2018.
- Lamborg, C. H., Hammerschmidt, C. R., Bowman, K. L., Swarr, G. J., Munson, K. M., Ohnemus, D. C.,
- 733 Lam, P. J., Heimburger, L. E., Rijkenberg, M. J., and Saito, M. A.: A global ocean inventory of
- 734 anthropogenic mercury based on water column measurements, Nature, 512, 65-68,
- 735 10.1038/nature13563, 2014.
- 736 Landis, M. S. and Keeler, G. J.: Atmospheric mercury deposition to Lake Michigan during the Lake
- 737 Michigan Mass Balance Study, Environmental science & technology, 36, 4518-4524,
- 738 10.1021/es011217b, 2002.
- 739 Laurier, F. and Mason, R.: Mercury concentration and speciation in the coastal and open ocean
- 740 boundary layer, J. Geophys. Res.-Atmos., 112, 10.1029/2006jd007320, 2007.
- Lavoie, R. A., Bouffard, A., Maranger, R., and Amyot, M.: Mercury transport and human exposure

- 742 from global marine fisheries, Scientific reports, 8, 10.1038/s41598-018-24938-3, 2018.
- Li, H., Huang, K., Fu, Q., Lin, Y., Chen, J., Deng, C., Tian, X., Tang, Q., Song, Q., and Wei, Z.: Airborne
- 744 black carbon variations during the COVID-19 lockdown in the Yangtze River Delta megacities
- 745 suggest actions to curb global warming, Environ Chem Lett, 1-10, 10.1007/s10311-021-01327-3,
- 746 2021
- 747 Li, H., Qin, X. F., Chen, J., Wang, G. C., Liu, C. F., Lu, D., Zheng, H. T., Song, X. Q., Gao, Q. Q., Xu, J.,
- 748 Zhu, Y. C., Liu, J. G., Wang, X. F., Deng, C. R., and Huang, K.: Continuous Measurement and
- 749 Molecular Compositions of Atmospheric Water-Soluble Brown Carbon in the Nearshore Marine
- 750 Boundary Layer of Northern China: Secondary Formation and Influencing Factors, J. Geophys.
- 751 Res.-Atmos., 128, 10.1029/2023jd038565, 2023.
- 752 Lin, C. J., Pan, L., Streets, D. G., Shetty, S. K., Jang, C., Feng, X., Chu, H. W., and Ho, T. C.: Estimating
- mercury emission outflow from East Asia using CMAQ-Hg, Atmos. Chem. Phys., 10, 1853-1864,
- 754 10.5194/acp-10-1853-2010, 2010.
- 755 Lindberg, S. E., Hanson, P. J., Meyers, T. P., and Kim, K. H.: Air/surface exchange of mercury vapor
- 756 over forests The need for a reassessment of continental biogenic emissions, Atmospheric
- 757 Environment, 32, 895-908, 10.1016/s1352-2310(97)00173-8, 1998.
- 758 Liu, K., Wu, Q., Wang, L., Wang, S., Liu, T., Ding, D., Tang, Y., Li, G., Tian, H., Duan, L., Wang, X., Fu,
- 759 X., Feng, X., and Hao, J.: Measure-Specific Effectiveness of Air Pollution Control on China's
- 760 Atmospheric Mercury Concentration and Deposition during 2013-2017, Environmental science &
- 761 technology, 53, 8938-8946, 10.1021/acs.est.9b02428, 2019.
- 762 Liu, M., Chen, L., Wang, X., Zhang, W., Tong, Y., Ou, L., Xie, H., Shen, H., Ye, X., Deng, C., and Wang,
- 763 H.: Mercury export from mainland China to adjacent seas and its influence on the marine mercury
- 764 balance, Environ. Sci. Technol., 50, 6224, 2016.
- 765 Luo, W., Wang, T., Jiao, W., Hu, W., Naile, J. E., Khim, J. S., Giesy, J. P., and Lu, Y.: Mercury in coastal
- 766 watersheds along the Chinese Northern Bohai and Yellow Seas, Journal of Hazardous Materials,
- 767 215-216, 199-207, https://doi.org/10.1016/j.jhazmat.2012.02.052, 2012.
- 768 Mao, H., Cheng, I., and Zhang, L.: Current understanding of the driving mechanisms for
- 769 spatiotemporal variations of atmospheric speciated mercury: a review, Atmos. Chem. Phys., 16,
- 770 12897-12924, 10.5194/acp-16-12897-2016, 2016.
- 771 Mason, R. P.: Mercury emissions from natural processes and their importance in the global mercury
- 772 cycle, in: Mercury Fate and Transport in the Global Atmosphere: Emissions, Measurements and
- Models, edited by: Mason, R., and Pirrone, N., Springer US, Boston, MA, 173-191, 10.1007/978-0-
- 774 387-93958-2\_7, 2009.
- Mason, R. P., Lawson, N. M., and Sheu, G. R.: Mercury in the Atlantic Ocean: factors controlling air-
- 776 sea exchange of mercury and its distribution in the upper waters, Deep Sea Research Part II: Topical
- 777 Studies in Oceanography, 48, 2829-2853, https://doi.org/10.1016/S0967-0645(01)00020-0, 2001.
- 778 Mason, R. P., Hammerschmidt, C. R., Lamborg, C. H., Bowman, K. L., Swarr, G. J., and Shelley, R. U.:
- 779 The air-sea exchange of mercury in the low latitude Pacific and Atlantic Oceans, Deep-Sea
- 780 Research Part I-Oceanographic Research Papers, 122, 17-28, 10.1016/j.dsr.2017.01.015, 2017.
- 781 Mason, R. P., Choi, A. L., Fitzgerald, W. F., Hammerschmidt, C. R., Lamborg, C. H., Soerensen, A. L.,
- and Sunderland, E. M.: Mercury biogeochemical cycling in the ocean and policy implications,
- 783 Environmental Research, 119, 101-117, 10.1016/j.envres.2012.03.013, 2012.
- Mastromonaco, M. G. N., Gardfeldt, K., Assmann, K. M., Langer, S., Delali, T., Shlyapnikov, Y. M.,
- 785 Zivkovic, I., and Horvat, M.: Speciation of mercury in the waters of the Weddell, Amundsen and

- 786 Ross Seas (Southern Ocean), Mar. Chem., 193, 20-33, 10.1016/j.marchem.2017.03.001, 2017.
- Nightingale, P. D., Malin, G., Law, C. S., Watson, A. J., Liss, P. S., Liddicoat, M. I., Boutin, J., and
- 788 Upstill-Goddard, R. C.: In situ evaluation of air-sea gas exchange parameterizations using novel
- 789 conservative and volatile tracers, 14, 373-387, https://doi.org/10.1029/1999GB900091, 2000.
- 790 O'Driscoll, N. J., Siciliano, S. D., Lean, D. R. S., and Amyot, M.: Gross Photoreduction Kinetics of
- 791 Mercury in Temperate Freshwater Lakes and Rivers: Application to a General Model of DGM
- 792 Dynamics, Environmental science & technology, 40, 837-843, 10.1021/es051062y, 2006.
- 793 O'Driscoll, N. J., Beauchamp, S., Siciliano, S. D., Rencz, A. N., and Lean, D. R. S.: Continuous Analysis
- 794 of Dissolved Gaseous Mercury (DGM) and Mercury Flux in Two Freshwater Lakes in Kejimkujik Park,
- 795 Nova Scotia: Evaluating Mercury Flux Models with Quantitative Data, Environmental science &
- 796 technology, 37, 2226-2235, 10.1021/es025944y, 2003.
- 797 Obrist, D., Kirk, J. L., Zhang, L., Sunderland, E. M., Jiskra, M., and Selin, N. E.: A review of global
- 798 environmental mercury processes in response to human and natural perturbations: Changes of
- 799 emissions, climate, and land use, Ambio, 47, 116-140, 10.1007/s13280-017-1004-9, 2018.
- 800 Osterwalder, S., Nerentorp, M., Zhu, W., Jiskra, M., Nilsson, E., Nilsson, M. B., Rutgersson, A.,
- 801 Soerensen, A. L., Sommar, J., Wallin, M. B., Wängberg, I., and Bishop, K.: Critical Observations of
- 802 Gaseous Elemental Mercury Air Sea Exchange, Global Biogeochemical Cycles, 35,
- 803 10.1029/2020gb006742, 2021.
- Outridge, P. M., Mason, R. P., Wang, F., Guerrero, S., and Heimbürger-Boavida, L. E.: Updated
- 805 Global and Oceanic Mercury Budgets for the United Nations Global Mercury Assessment 2018,
- 806 Environmental science & technology, 52, 11466-11477, 10.1021/acs.est.8b01246, 2018.
- 807 Paatero, P. and Tapper, U.: POSITIVE MATRIX FACTORIZATION A NONNEGATIVE FACTOR
- 808 MODEL WITH OPTIMAL UTILIZATION OF ERROR-ESTIMATES OF DATA VALUES, Environmetrics,
- 809 5, 111-126, 10.1002/env.3170050203, 1994.
- Pacyna, E. G., Pacyna, J. M., Steenhuisen, F., and Wilson, S.: Global anthropogenic mercury emission
- 811 inventory for 2000, Atmospheric Environment, 40, 4048-4063, 10.1016/j.atmosenv.2006.03.041,
- 812 2006
- 813 Pacyna, E. G., Pacyna, J. M., Sundseth, K., Munthe, J., Kindbom, K., Wilson, S., Steenhuisen, F., and
- Maxson, P.: Global emission of mercury to the atmosphere from anthropogenic sources in 2005
- 815 and projections to 2020, Atmospheric Environment, 44, 2487-2499,
- 816 10.1016/j.atmosenv.2009.06.009, 2010.
- Pacyna, J. M., Travnikov, O., De Simone, F., Hedgecock, I. M., Sundseth, K., Pacyna, E. G.,
- 818 Steenhuisen, F., Pirrone, N., Munthe, J., and Kindbom, K.: Current and future levels of mercury
- atmospheric pollution on a global scale, Atmos. Chem. Phys., 16, 12495-12511, 10.5194/acp-16-
- 820 12495-2016, 2016.
- 821 Pirrone, N., Cinnirella, S., Feng, X., Finkelman, R. B., Friedli, H. R., Leaner, J., Mason, R., Mukherjee,
- 822 A. B., Stracher, G. B., Streets, D. G., and Telmer, K.: Global mercury emissions to the atmosphere
- from anthropogenic and natural sources, Atmos. Chem. Phys., 10, 5951-5964, 10.5194/acp-10-
- 824 5951-2010, 2010.
- 825 Poissant, L., Amyot, M., Pilote, M., and Lean, D.: Mercury Water-Air Exchange over the Upper St.
- 826 Lawrence River and Lake Ontario, Environmental science & technology, 34, 3069-3078,
- 827 10.1021/es990719a, 2000.
- 828 Qin, X., Wang, F., Deng, C., Wang, F., and Yu, G.: Seasonal variation of atmospheric particulate

- 829 mercury over the East China Sea, an outflow region of anthropogenic pollutants to the open Pacific
- 830 Ocean, Atmos. Pollut. Res., 7, 876-883, 10.1016/j.apr.2016.05.004, 2016.
- 831 Qin, X., Wang, X., Shi, Y., Yu, G., Zhao, N., Lin, Y., Fu, Q., Wang, D., Xie, Z., Deng, C., and Huang, K.:
- 832 Characteristics of atmospheric mercury in a suburban area of east China: sources, formation
- 833 mechanisms, and regional transport, Atmos. Chem. Phys., 19, 5923-5940, 10.5194/acp-19-5923-
- 834 2019, 2019.
- 835 Qin, X., Zhang, L., Wang, G., Wang, X., Fu, Q., Xu, J., Li, H., Chen, J., Zhao, Q., Lin, Y., Huo, J., Wang,
- 836 F., Huang, K., and Deng, C.: Assessing contributions of natural surface and anthropogenic
- 837 emissions to atmospheric mercury in a fast-developing region of eastern China from 2015 to 2018,
- 838 Atmos. Chem. Phys., 20, 10985-10996, 10.5194/acp-20-10985-2020, 2020.
- 839 Selin, N. E.: Global Biogeochemical Cycling of Mercury: A Review, Annu. Rev. Environ. Resour., 34,
- 840 43-63, 10.1146/annurev.environ.051308.084314, 2009.
- 841 Soerensen, A. L., Mason, R. P., Balcom, P. H., and Sunderland, E. M.: Drivers of Surface Ocean
- 842 Mercury Concentrations and Air–Sea Exchange in the West Atlantic Ocean, Environmental science
- 843 & technology, 47, 7757-7765, 10.1021/es401354q, 2013.
- 844 Soerensen, A. L., Skov, H., Jacob, D. J., Soerensen, B. T., and Johnson, M. S.: Global Concentrations
- 845 of Gaseous Elemental Mercury and Reactive Gaseous Mercury in the Marine Boundary Layer,
- 846 Environmental science & technology, 44, 7425-7430, 10.1021/es903839n, 2010a.
- Soerensen, A. L., Mason, R. P., Balcom, P. H., Jacob, D. J., Zhang, Y. X., Kuss, J., and Sunderland, E.
- 848 M.: Elemental Mercury Concentrations and Fluxes in the Tropical Atmosphere and Ocean,
- 849 Environmental science & technology, 48, 11312-11319, 10.1021/es503109p, 2014.
- 850 Soerensen, A. L., Sunderland, E. M., Holmes, C. D., Jacob, D. J., Yantosca, R. M., Skov, H., Christensen,
- 3. H., Strode, S. A., and Mason, R. P.: An Improved Global Model for Air-Sea Exchange of Mercury:
- 852 High Concentrations over the North Atlantic, Environmental science & technology, 44, 8574-8580,
- 853 10.1021/es102032g, 2010b.
- 854 Sprovieri, F., Pirrone, N., Bencardino, M., D'Amore, F., Carbone, F., Cinnirella, S., Mannarino, V.,
- 855 Landis, M., Ebinghaus, R., Weigelt, A., Brunke, E. G., Labuschagne, C., Martin, L., Munthe, J.,
- 856 Wangberg, I., Artaxo, P., Morais, F., de Melo Jorge Barbosa, H., Brito, J., Cairns, W., Barbante, C.,
- Del Carmen Dieguez, M., Garcia, P. E., Dommergue, A., Angot, H., Magand, O., Skov, H., Horvat,
- 858 M., Kotnik, J., Read, K. A., Neves, L. M., Gawlik, B. M., Sena, F., Mashyanov, N., Obolkin, V., Wip, D.,
- 859 Feng, X. B., Zhang, H., Fu, X., Ramachandran, R., Cossa, D., Knoery, J., Marusczak, N., Nerentorp,
- $860 \qquad \text{M., and Norstrom, C.: Atmospheric mercury concentrations observed at ground-based monitoring} \\$
- 861 sites globally distributed in the framework of the GMOS network, Atmos Chem Phys, 16, 11915 -
- 862 11935, 10.5194/acp-16-11915-2016, 2016.
- 863 Streets, D. G., Devane, M. K., Lu, Z. F., Bond, T. C., Sunderland, E. M., and Jacob, D. J.: All-Time
- 864 Releases of Mercury to the Atmosphere from Human Activities, Environmental science &
- 865 technology, 45, 10485-10491, 10.1021/es202765m, 2011.
- Viana, M., Amato, F., Alastuey, A., Querol, X., Moreno, T., García Dos Santos, S., Herce, M. D., and
- 867 Fernández-Patier, R.: Chemical Tracers of Particulate Emissions from Commercial Shipping,
- 868 Environmental science & technology, 43, 7472-7477, 10.1021/es901558t, 2009.
- Wang, C., Wang, Z., and Zhang, X.: Characteristics of mercury speciation in seawater and emission
- 870 flux of gaseous mercury in the Bohai Sea and Yellow Sea, Environ Res, 182, 109092,
- 871 10.1016/j.envres.2019.109092, 2020.
- Wang, C., Ci, Z., Wang, Z., and Zhang, X.: Air-sea exchange of gaseous mercury in the East China

- 873 Sea, Environ Pollut, 212, 535-543, 10.1016/j.envpol.2016.03.016, 2016a.
- Wang, C., Wang, Z., Hui, F., and Zhang, X.: Speciated atmospheric mercury and sea-air exchange
- of gaseous mercury in the South China Sea, Atmospheric Chemistry and Physics, 19, 10111-10127,
- 876 10.5194/acp-19-10111-2019, 2019a.
- Wang, C., Wang, Z., Hui, F., and Zhang, X.: Speciated atmospheric mercury and sea-air exchange
- 878 of gaseous mercury in the South China Sea, Atmospheric Chemistry and Physics, 19, 10111-10127,
- 879 10.5194/acp-19-10111-2019, 2019b.
- 880 Wang, C., Wang, Z., Ci, Z., Zhang, X., and Tang, X.: Spatial-temporal distributions of gaseous
- 881 element mercury and particulate mercury in the Asian marine boundary layer, Atmospheric
- 882 Environment, 126, 107-116, 10.1016/j.atmosenv.2015.11.036, 2016b.
- 883 Wang, G. C., Chen, J., Xu, J., Yun, L., Zhang, M. D., Li, H., Qin, X. F., Deng, C. R., Zheng, H. T., Gui, H.
- 884 Q., Liu, J. G., and Huang, K.: Atmospheric Processing at the Sea-Land Interface Over the South
- 885 China Sea: Secondary Aerosol Formation, Aerosol Acidity, and Role of Sea Salts, J. Geophys. Res.-
- 886 Atmos., 127, 10.1029/2021jd036255, 2022.
- 887 Wang, X., Lin, C. J., and Feng, X.: Sensitivity analysis of an updated bidirectional air-surface
- 888 exchange model for elemental mercury vapor, Atmospheric Chemistry and Physics, 14, 6273-6287,
- 889 10.5194/acp-14-6273-2014, 2014.
- 890 Wang, X., Lin, C.-J., Feng, X., Yuan, W., Fu, X., Zhang, H., Wu, Q., and Wang, S.: Assessment of
- 891 Regional Mercury Deposition and Emission Outflow in Mainland China, 123, 9868-9890,
- 892 <u>https://doi.org/10.1029/2018JD028350</u>, 2018.
- 893 Wangberg, I., Schmolke, S., Schager, P., Munthe, J., Ebinghaus, R., and Iverfeldt, A.: Estimates of
- 894 air-sea exchange of mercury in the Baltic Sea, Atmospheric Environment, 35, 5477-5484,
- 895 10.1016/s1352-2310(01)00246-1, 2001.
- 896 Wanninkhof and Oceans, R. J. J. o. G. R.: Relationship between wind speed and gas exchange over
- 897 the ocean, 97, 7373, 1992.
- 898 Wanninkhof, R.: RELATIONSHIP BETWEEN WIND-SPEED AND GAS-EXCHANGE OVER THE OCEAN,
- 899 Journal of Geophysical Research-Oceans, 97, 7373-7382, 10.1029/92jc00188, 1992.
- 900 Wanninkhof, R.: Relationship between wind speed and gas exchange over the ocean revisited,
- 901 Limnology and Oceanography-Methods, 12, 351-362, 10.4319/lom.2014.12.351, 2014.
- 902 Wu, X., Fu, X., Zhang, H., Tang, K., Wang, X., Zhang, H., Deng, Q., Zhang, L., Liu, K., Wu, Q., Wang,
- 903 S., and Feng, X.: Changes in Atmospheric Gaseous Elemental Mercury Concentrations and Isotopic
- 904 Compositions at Mt. Changbai During 2015–2021 and Mt. Ailao During 2017–2021 in China,
- Journal of Geophysical Research: Atmospheres, 128, 10.1029/2022jd037749, 2023.
- 906 Zhang, L., Wang, S., Wang, L., Wu, Y., Duan, L., Wu, Q., Wang, F., Yang, M., Yang, H., Hao, J., and
- 907 Liu, X.: Updated emission inventories for speciated atmospheric mercury from anthropogenic
- 908 sources in China, Environmental science & technology, 49, 3185-3194, 10.1021/es504840m, 2015.
- Zhang, Y., Jacob, D. J., Horowitz, H. M., Chen, L., Amos, H. M., Krabbenhoft, D. P., Slemr, F., St Louis,
- 910 V. L., and Sunderland, E. M.: Observed decrease in atmospheric mercury explained by global
- 911 decline in anthropogenic emissions, Proc Natl Acad Sci U S A, 113, 526-531,
- 912 10.1073/pnas.1516312113, 2016.
- 213 Zhu, W., Lin, C. J., Wang, X., Sommar, J., Fu, X., and Feng, X.: Global observations and modeling of
- 914 atmosphere-surface exchange of elemental mercury: a critical review, Atmos. Chem. Phys., 16,
- 915 4451-4480, 10.5194/acp-16-4451-2016, 2016.